# Sulfate Promotion of Selective Catalytic Reduction of Nitric Oxide by Ammonia on Ceria

SCHOLARONE™
Manuscripts

**Sulfate Promotion of Selective Catalytic Reduction of Nitric Oxide by Ammonia on Ceria**

Linxiao Chen, Vaibhav Agrawal,[†] and Steven L. Tait*

## Abstract

Selective catalytic reduction of nitric oxide by ammonia ($NH_3$-SCR) is a promising technology for $NO_x$ emission control. In this work, the recently discovered sulfate promotion effect in this reaction was thoroughly investigated on ceria. Sulfates derived from different organic S precursors all exhibit a promotion effect. Mechanistic studies generate a reaction network including both Langmuir-Hinshelwood and Eley-Rideal mechanisms. Sulfates were shown to be versatile promoters with multiple functions: they tune the adsorption of reactants towards a more balanced intermediate coverage by creating strong Lewis acid sites, facilitate *$NH_2$ formation, and suppress ammonia oxidation through surface oxygen deactivation. The comparison between sulfates and the classic inorganic promoter $FeO_x$ revealed that sulfates are more effective, especially at high temperature. This is mainly attributed to the high coverages of Eley-Rideal intermediates and low ammonia oxidation activity on sulfated ceria. This work provides fundamental understanding of the role of surface sulfates in $NH_3$-SCR, which are essential under actual operation conditions. This understanding presents an exciting opportunity for future catalyst design with high durability and low cost.

**Keywords**: $NH_3$-SCR; sulfate promotion; reaction mechanism; *in situ* DRIFT

Dept. of Chemistry, Indiana University, Bloomington, Indiana 47405, U. S. A.

* E-mail: tait@indiana.edu, Tel.: +1-812-855-1302

[†] Present address: Indian Institute of Technology, Roorkee, India

## Introduction

The emission of low-concentration NO from stationary and mobile sources poses serious threats to the environment and human health. Recently, selective catalytic reduction of NO by $NH_3$ ($NH_3$-SCR) has been regarded as a promising technology to solve this problem. This process, if properly catalyzed, could lead to 100% $N_2$ selectivity at reasonably low temperature.[1] Mixed oxides,[2-15] such as the current commercial catalyst $VO_x$-$WO_x$($MO_x$)/$TiO_2$[16-19] and Fe(Cu)-exchanged zeolites[20-27] are two types of catalysts that are most heavily investigated. The reducibility of catalyst surfaces, and the abundance of Lewis and/or Brønsted acid sites are crucial to achieve high activity. However, these catalysts all have significant drawbacks, such as narrow operational temperature window,[28, 29] instability under harsh conditions, low resistance towards $SO_2$,[30, 31] and high cost. Therefore, demands for new efficient, inexpensive, and robust $NH_3$-SCR catalyst still exists.

The mechanism of $NH_3$-SCR has been studied for decades, but some aspects remain unclear due to multiple active sites and reaction pathways. Both Langmuir-Hinshelwood (L-H, both $NH_3$ and NO adsorb onto catalysts)[1, 32-34] and Eley-Rideal (E-R, NO stays in gas phase)[1, 35-37] mechanisms have been proposed (see **Scheme 1**) and, in some cases, both types of mechanism are active.[1, 34-36] On mixed oxides such as Eu/Mn/$TiO_x$, Sm/$MnO_x$, and $SO_2$-treated $CeO_2$, Lewis acid sites are often viewed as active sites through molecularly adsorbed *$NH_3$ intermediate, but there has been evidence supporting that Brønsted acid sites also participate in the reaction.[35-37] Recent developments in metal oxide catalysts have allowed $NH_3$-SCR at temperatures as low as 100 °C.[38-42] On zeolite systems such as H/ZSM-5, Fe/ZSM-5, and Fe/SSZ-13, Brønsted acid sites are more likely active sites with *$NH_4^+$ intermediate.[22, 24, 32, 33, 43] They have been more credited for low-temperature activity (< 200 °C) because of the high reactivity of *$NH_4^+$ intermediate.[29,

[44-46] The picture is further complicated by the presence of the fast-SCR pathway, in which NO is first oxidized into $NO_2$ on surfaces.[32, 33, 43, 47, 48] Meanwhile, several potential side reactions could happen, such as unselective reduction of NO generating $N_2O$ through Eley-Rideal mechanism[21, 34] and oxidation of $NH_3$ to NO or $N_2$.[37, 49-52] The $NH_3$ oxidation reactions become important especially at high temperature. For a specific catalyst, which reaction pathway dominates and what types of active sites/intermediates are involved are difficult to predict and in a lot of cases under debates.
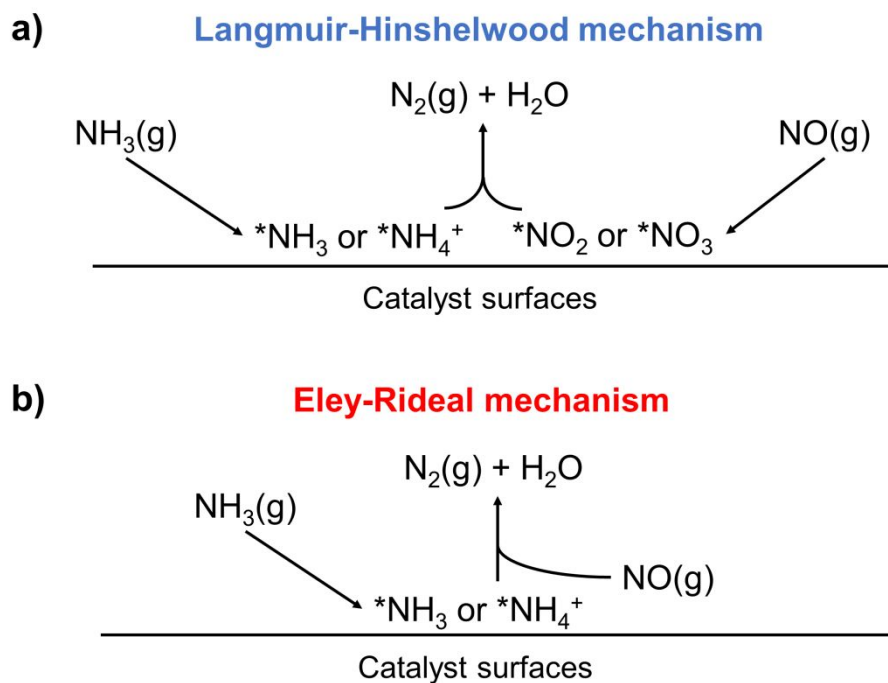


**Scheme 1.** Generalized mechanisms of $NH_3$-SCR reported in literature: **(a)** Langmuir-Hinshelwood mechanism and **(b)** Eley-Rideal mechanism. The key difference between two mechanisms is whether NO adsorbs onto the catalyst surface (L-H) or not (E-R).

Due to its reducibility, abundance of Lewis acid sites, and low cost, $CeO_2$ has received significant attention for $NH_3$-SCR as a catalyst,[37, 44, 53, 54] a support material,[12, 29, 53, 55] or a promoter.[48, 53, 56-58] Despite its versatile capability, bare $CeO_2$ itself, without the addition of any

promoters, is almost inert.[34, 37, 53] In fact, most metal oxides catalysts require promoters to achieve satisfactory activity for $NH_3$-SCR.[29, 36, 59-62] The most commonly applied type of promoter is another transition metal oxide,[18, 30, 61, 63-68] often $WO_x$ or $MO_x$. $FeO_x$ has also been widely investigated as a promoter for $NH_3$-SCR and other SCR technologies because it provides Lewis acid sites and reducibility.[2, 18, 55, 66, 69-71] In addition to modifying surface acidity and/or reducibility, promoters may also prevent catalyst sintering. In the past decade, it has also been recognized that surface sulfates can promote $NH_3$-SCR activity by forming new active phases, enhancing surface acidity, and/or suppressing active surface oxygen in $NH_3$ oxidation side reactions.[17, 37, 60, 72-74] Recent work by Li and Schwank, *et al*., revealed the role of sulfates and shape dependence in $CeO_2$-catalyzed $NH_3$-SCR.[75] The discovery of the sulfate promotion effect opened new opportunities for effective SCR catalyst design because sulfates are less expensive than metal oxide clusters, tend to be more stable with high-water-content feed at elevated temperature, and are resistant to $SO_x$ poisoning.[10, 31, 73, 76] Consequently, more detailed fundamental understanding of sulfate promotion is desired to further improve SCR catalysis.

In this work, we investigated the sulfate promotion effect on $CeO_2$-catalyzed $NH_3$-SCR in detail and compared it with a more traditional metal oxide promoter, $FeO_x$. The sulfate promotion effect was verified using various S precursors. It was proved to be valid on different surfaces, and stronger than $FeO_x$. Thorough *in situ* Diffuse Reflectance Infrared Fourier-Transform Spectroscopy (DRIFTS) studies provided deep insight into the reaction mechanism, revealing that sulfates promote both L-H and E-R mechanisms, and suppress the $NH_3$ oxidation side reaction. The unique capability to create stronger Lewis acid sites, increase surface basicity, and deactivate surface oxygen simultaneously is the crucial reason that sulfates are more effective promoters than $FeO_x$. Fundamental understanding obtained in this study is valuable for

instructing designs of novel SCR promoters. Mechanistic studies presented here also elucidate roles of surface sulfates in this reaction, which are common with $SO_x$-containing feed.

## Experimental

### Preparation and characterization of promoted CeO$_2$

S-containing ligands used in this work include 2-pyridinesulfonic acid (2-PSA, Sigma Aldrich, 97%, **Figure 1a**) 3-pyridinesulfonic acid (3-PSA, Sigma Aldrich, 98%, **Figure S2b**), benzenesulfonic acid (BSA, Sigma Aldrich, **Figure S2c**), methanesulfonic acid (MSA, Sigma Aldrich, 99%, **Figure S2d**), and ammonium sulfate (AS, Macron, ACS grade). We selected these as a series of simple organic sulfur precursors that will not introduce any metal cations to the catalyst. MSA is the simplest organic precursor and will likely not leave any organic fragments. BSA and PSA have aromatic side chains that may create organic fragments with N (PSA) or without N (BSA). The difference between 2-PSA and 3-PSA is the position of the $-SO_3H$ group on the pyridine ring. These variations are aimed at examining whether the promotion effect depends on precursor structure and investigating potential effects from residual organic fragments. The synthesis of promoted CeO$_2$ catalysts follows a wet impregnation procedure. CeO$_2$ powder (99.9%, Alfa Aesar, BET surface area $\approx$ 5 m$^2$/g) was prepared in one of two states, reduced or oxidized, by annealing at 400 °C for 4 h in a 40 SCCM flow of either H$_2$ or O$_2$, respectively.  0.3 g CeO$_2$ powder was suspended in 20 mL water, then 5 mL solution of 80 mmol S-containing molecules into the mixture. The final mixture was stirred for 3 h, then dried at 100 °C overnight. The dry catalyst powders were then washed with water and DCM, then activated at 350 °C under 8% O$_2$

FeO$_x$/CeO$_2$ catalysts were prepared in the same way, except that 0.0034 g FeCl$_2$ (0.5 Fe wt%, Alfa Aesar) was added in the wet impregnation step (instead of an S-containing molecule) and following the final rinsing, the catalyst was calcined under dry air flow (instead of O$_2$) at 400 °C for 4 h. The loading of Fe was verified by atomic adsorption spectroscopy.

X-ray photoemission spectra (XPS) were recorded with a PHI Versaprobe II XPS spectrometer using a monochromated Al Kα X-ray source at the Ce 3$d$, O 1$s$, S 2$p$, C 1$s$, and Cl 2$p$ regions on all samples, plus Fe 2$p$ and Fe 3$p$ regions on FeO$_x$/CeO$_2$ samples. Catalyst powders were held on a sample platen using double-stick tape and analyzed using the PHI dual charge neutralization mode. The binding energy (BE) was corrected with the main Ce 3$d$ 5/2 peak (882.4 eV) because of its sharp shape and high intensity. After correction, the BE of C 1$s$ peak was checked, which is within 0.1 eV of 284.8 eV on all samples. Backgrounds from bare CeO$_2$ were properly subtracted from original spectra before analysis.

CO adsorption experiments were conducted at room temperature. Catalysts were exposed to 10% CO (balanced with Ar, total flow rate = 40 SCCM) for 30 min, and then a DRIFT spectrum was collected under CO flow to monitor adsorption of CO on surfaces. The DRIFTS cell was then purged by pure Ar for 60 min to evacuate CO gas, and another DRIFT spectrum was collected under Ar flow to detect irreversibly-adsorbed CO. The background was collected before CO exposure under pure Ar flow.

**Catalytic activity tests**

NH$_3$-SCR activities were tested in a customized flow reactor (described previously).[77] 100 mg catalyst were used in all experiments. The reaction mixture contained 23 SCCM NH$_3$ (1000

ppm, balanced with Ar, Airgas), 23 SCCM NO (1000 ppm, balanced with $N_2$, Airgas), and 4

SCCM $O_2$ (Airgas, 99.9%), which is equivalent with 50 SCCM total flow with 460 ppm $NH_3$,

460 ppm NO, and 8% $O_2$. We note that the space velocity of these measurements are lower than

common industrial operation conditions due to limitations of our reactor, however, these

conditions are suitable to highlight the promotion effect and study it systematically. A mass

spectrometer was used to detect post-reaction gas composition: $m/z = 30$ signal was monitored to

represent NO and potential by-products $N_2O$ ($m/z = 44$) and $NO_2$ ($m/z = 46$) were also monitored.

Before each temperature programmed reaction (TPR) trial, the limits on $m/z = 30$ intensity were

checked: maximum intensity, $i.e.$, no NO conversion ($NO_{no\text{-}conv}$), was measured by replacing

$NH_3$/Ar in the stream with pure Ar (Airgas, 99.999%) and the $m/z = 30$ intensity with no NO in

the stream (100% conversion situation, $NO_{full\text{-}conv}$) was measured by replacing $NO/N_2$ in the

stream with pure $N_2$ (Airgas, 99.9%). In each TPR trial, the reaction was performed at 200 °C,

250 °C, 300 °C, and 350 °C. The NO conversion was calculated from the following equation

using $m/z = 30$ intensity ($NO_{reaction}$):

$$NO\ conversion = 1 - \frac{NO_{reaction} - NO_{full-conv}}{NO_{no-conv} - NO_{full-conv}}$$

$NH_3$ oxidation reactions were also tested in the same flow reactor. 100 mg catalysts were

used in all experiments. The reaction mixture was the same as for the $NH_3$-SCR reaction, except

that $NO/N_2$ was replaced with pure $N_2$: 50 SCCM total flow with 460 ppm $NH_3$ and 8% $O_2$. The

$NH_3$ conversion is difficult to quantify due to large $H_2O$ contribution to the $m/z = 17$ peak and $O_2$

contribution to $m/z = 16$ peak. Therefore, potential products NO, $N_2O$, and $NO_2$ were monitored

using $m/z = 30$, 44, and 46 respectively. The other possible product, $N_2$, is also difficult to

quantify because of high background level from air. Each TPR trial also included reaction at

200 °C, 250 °C, 300 °C, and 350 °C. Before each TPR trial, a control measurement of minimum NO ($m/z$ = 30) intensity, *i.e.*, no $NH_3$ to NO conversion ($NO_{no\text{-}NH3\text{-}conv}$), was made by replacing $NH_3$/Ar with pure Ar. Maximum $m/z$ = 30 intensity, *i.e.*, full $NH_3$ to NO conversion ($NO_{full\text{-}NH3\text{-}conv}$), was measured by replacing $NH_3$/Ar with pure Ar and $N_2$ with NO/$N_2$, such that the NO flow in this control measurement is a 1:1 mole ratio with the $NH_3$ flow in the reaction experiment. The $NH_3$ conversion to NO was calculated using $m/z$ = 30 intensity ($NO_{NH3\text{-}reaction}$) by the equation:

$$NH_3\ Converion\ (to\ NO) = \frac{NO_{NH_3-reaction} - NO_{no-NH_3-conv}}{NO_{full-NH_3-conv} - NO_{no-NH_3-conv}}$$

### *In situ* DRIFTS experiments

*In situ* DRIFTS experiments were carried out with a DiffuseIR Environmental Chamber (PIKE Technologies, 162-4160, HTV). Before experiments, $CeO_2$ and $FeO_x$/$CeO_2$ catalysts were cleaned with 10% $O_2$ at 400 °C for 30 min to get rid of surface contaminations. 2-PSA/$CeO_2$ catalyst was activated by 8% $O_2$ at 350 °C for 30 min. In all experiments, the total gas flow rate was 40 SCCM. DRIFT spectra were collected with a Magna 550 FTIR spectrometer (Nicolet) and presented in the Kubelka-Munk form. For $NH_3$ adsorption, NO + $O_2$ adsorption, and steady-state experiments, spectra shown in this work are averages of 500 scans. For transient experiments, spectra shown are averages of 100 scans for better time resolution. Backgrounds were collected at the same temperature, under pure Ar flow for 500 scans.

## Results & discussion

### 1. Synthesis, activation, and characterization of sulfated CeO$_2$

Sulfated CeO$_2$ was synthesized by impregnating CeO$_2$ with S-containing molecules, such as 2-pyridinesulfonic acid (2-PSA, **Figure 1a**), in water, followed by activation at 350 °C under 8% O$_2$. Before O$_2$ activation, XPS (**Table 1**) shows a 1:1 atomic ratio between N and S (N : Ce = 0.031 and S : Ce = 0.030), indicating that the impregnation is successful and 2-PSA is intact. The S 2$p$ binding energy (168.6 eV) is between values reported for SO$_4^{2-}$ (+6 oxidation state, ~169.0 eV) and SO$_3^{2-}$ (+4 oxidation state, ~167.1 eV),, which is in line with the value for the −SO$_3$H group in 2-PSA.[78] Room-temperature NH$_3$ (g) exposure to fresh 2-PSA/CeO$_2$ produces no DRIFTS-detectable *NH$_3$ (1168 cm$^{-1}$, 1315 cm$^{-1}$, and 1602 cm$^{-1}$) or *NH$_4^+$ (1460 cm$^{-1}$) species (**Figure S1**), suggesting the absence of Lewis acid sites (*NH$_3$) and Brønsted acid sites (*NH$_4^+$), which are supposed to provide binding sites for NH$_3$.[6, 46, 75] This implies (1) that the O-vacancies on CeO$_2$, which would have been Lewis acid sites for NH$_3$ adsorption, are occupied by 2-PSA and (2) that the −SO$_3$H group of 2-PSA, which would have been a Brønsted acid site for NH$_3$ adsorption, is consumed. Meanwhile, control experiments show that pyridine alone does not stick to CeO$_2$. Therefore, we speculate that during the impregnation, de-protonated 2-PSA first bind with Ce(III) sites at O-vacancies with the −SO$_3^-$ group (**Figure 1c, top**). After O-vacancies are saturated, 2-PSA may be able to bind with some Ce(IV) sites in a similar manner.
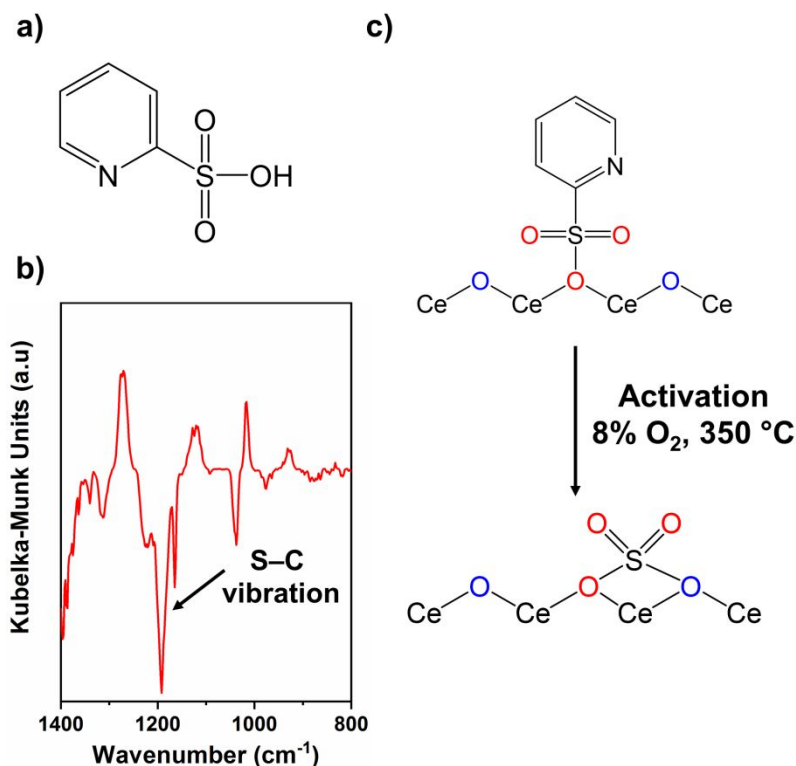
**Figure 1. (a)** Structure of 2-pydinesulfonic acid (2-PSA). **(b)** DRIFT spectrum of 2-PSA/CeO$_2$ after O$_2$ activation at 350 °C (background was collected before O$_2$ activation). **(c)** Proposed binding between 2-PSA and CeO$_2$ and the formation of surface sulfate upon activation.

After O$_2$ activation of 2-PSA/CeO$_2$, we observed a negative feature corresponding with S–C vibration in DRIFTS (**Figure 1b**). The XPS N : Ce ratio decreases to one third (from 0.031 to 0.012, **Table 1**), while the S : Ce ratio remains constant. Activation of 3-PSA/CeO$_2$ leads to qualitatively similar changes (N drops to one half instead of one third). The S $2p$ XPS peak slightly shifts toward higher binding energy (169.0 eV), consistent with the sulfate (SO$_4^{2-}$, S in +6 oxidation state) group. These results indicate that during O$_2$ activation, the S–C bond in 2-PSA breaks. More surface O bind with S forming sulfates, and most N-containing fragments leave the surface. C-containing fragments are not distinguishable from adventitious C in XPS. We note that the temperature and O$_2$ concentration used for activation are identical with those of

the harshest reaction conditions we tested. The constant S content before and after activation confirms the stability of sulfates during catalysis. Sulfated $CeO_2$ were also synthesized using other S-containing molecules: 3-pyridinesulfonic acid (3-PSA), benzenesulfonic acid (BSA), methanesulfonic acid (MSA), and ammonium sulfate (AS). Structures of these sulfate precursors and XPS results can be found as **Figure S2** and **Table S1**. Sulfate deposition is successful with each of these molecules onto $CeO_2$, though with some variation in S : Ce ratio.

**Table 1.** XPS characterization of 2-PSA/$CeO_2$. Peak area ratios for N:Ce and S:Ce and binding energy (BE) values for N $1s$ and S $2p$.

| Catalyst status | N : Ce | S : Ce | N $1s$ BE (eV) | S $2p$ BE (eV) |
|---|---|---|---|---|
| Fresh | 0.031 | 0.030 | 399.7 | 168.6 |
| $O_2$-activated | 0.012 | 0.032 | 400.3 | 169.0 |

The impact of sulfates on $CeO_2$ surface properties were probed by DRIFTS measurements of CO adsorption on $O_2$-activated 2-PSA/$CeO_2$. **Figure 2** exhibits that CO exposure (room temperature, 30 min) on bare $CeO_2$ yields large amount of carbonates (1200 $cm^{-1}$ - 1700 $cm^{-1}$) from the interaction with active surface O, while no peaks representing CO adsorption on Lewis acid sites ($CO_{ads}$) are identified. The doublet features between 2000 $cm^{-1}$ and 2200 $cm^{-1}$ are from CO (g) vibration. In contrast, the same treatment does not create significant amounts of carbonates on sulfated $CeO_2$. Nonetheless, a $CO_{ads}$ feature at ~2000 $cm^{-1}$ was observed. DRIFT spectra were collected again after purging CO with Ar to measure the reversibility of CO adsorption: CO adsorption is reversible, while carbonate adsorption is not (**Figure S3)**. The difference in the CO reactivity of surfaces indicates that sulfates deactivate most active surface O on $CeO_2$,[76, 79, 80] and create new, stronger Lewis acid sites.[81-84]
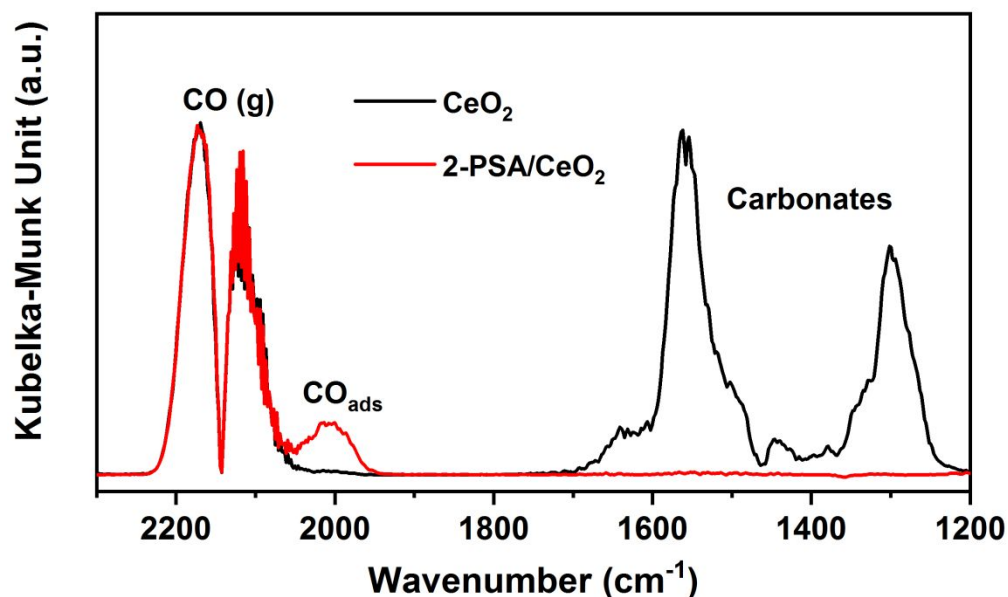
**Figure 2.** CO adsorption DRIFT spectra of bare $CeO_2$ (black) and activated 2-PSA/$CeO_2$ (red) showing the deactivation of active surface O and the creation of new, stronger Lewis acid sites after sulfate deposition.

## 2. $NH_3$-SCR and $NH_3$ oxidation activity of sulfated $CeO_2$ and $FeO_x$/$CeO_2$

The $NH_3$-SCR activity was tested for sulfated $CeO_2$ (after activation) from each S precursor. For comparison, we also tested the activity of bare $CeO_2$ and $CeO_2$ promoted with 0.5 wt% $FeO_x$ ($FeO_x$/$CeO_2$). **Figure 3** shows the NO conversion between 200 °C and 350 °C on all catalysts tested. (All catalysts were also tested at 150 °C but showed no activity. 350 °C was a sufficient upper limit to differentiate the behavior of the catalysts.) As shown in **Figure 3**, bare $CeO_2$ is only slightly active for $NH_3$-SCR at 300 °C (9% NO conversion). Although performing slightly differently from each other, all sulfated $CeO_2$ samples exhibit promoted activities across the entire temperature range tested. On all catalysts, the reaction is 100% selective towards $N_2$; we never detected the formation of potential by-products, $N_2O$ and $NO_2$. At low temperature, sulfated $CeO_2$ synthesized from pyridine-containing molecules, 2-PSA and 3-PSA, exhibit higher activities than others, although 3-PSA performs worse at high temperature. This is likely due to

the presence of N-containing fragments. The promotion effect of surface sulfates is significantly stronger than the inorganic promoter $FeO_x$, especially at high temperature (less than 50% NO conversion on $FeO_x/CeO_2$ at above 300 °C). The $FeO_x/CeO_2$ used in this work has 0.5 wt% Fe and the activity does not increase with higher $FeO_x$ loadings (1% or 5%). We note that the Fe content on 0.5 wt% $FeO_x/CeO_2$ is at least four times as high as the S content on S-promoted $CeO_2$ (both calculated from XPS), which further proves the effectiveness of sulfate as the promoter. XPS measurements indicate that the Fe is mainly Fe(III) based on the Fe $2p_{2/3}$ BE of 711.2 eV and that there is no residual Cl. The application of $FeO_x$ as a promoter for SCR or similar reactions has been widely investigated,[2, 18, 55, 66, 69-71] so we are impressed to see surface sulfates are more effective promoters than $FeO_x$. We also attempted to impregnate sulfates onto $FeO_x/CeO_2$ using 2-PSA, which exhibited similar activity as 2-PSA/$CeO_2$ without $FeO_x$. As the performance of different S precursors did not vary significantly, we decided to focus on 2-PSA/$CeO_2$ in the following mechanism study, which has the highest activity below 300 °C and relatively high activity at high temperature. The activity of 2-PSA/$CeO_2$ does not change under reaction conditions for up to 6 h, indicating good thermal stability of the catalyst. Co-feeding a small concentration of $H_2O$ by passing the NO/$N_2$ gas through a water bubbler does not impact the activity, implying 2-PSA/$CeO_2$ is not sensitive to low concentrations of $H_2O$. The promotion effect of 2-PSA-derived sulfates was also observed on reduced $CeO_2$, oxidized $CeO_2$, and $Fe_2O_3$ (**Figure S4**).
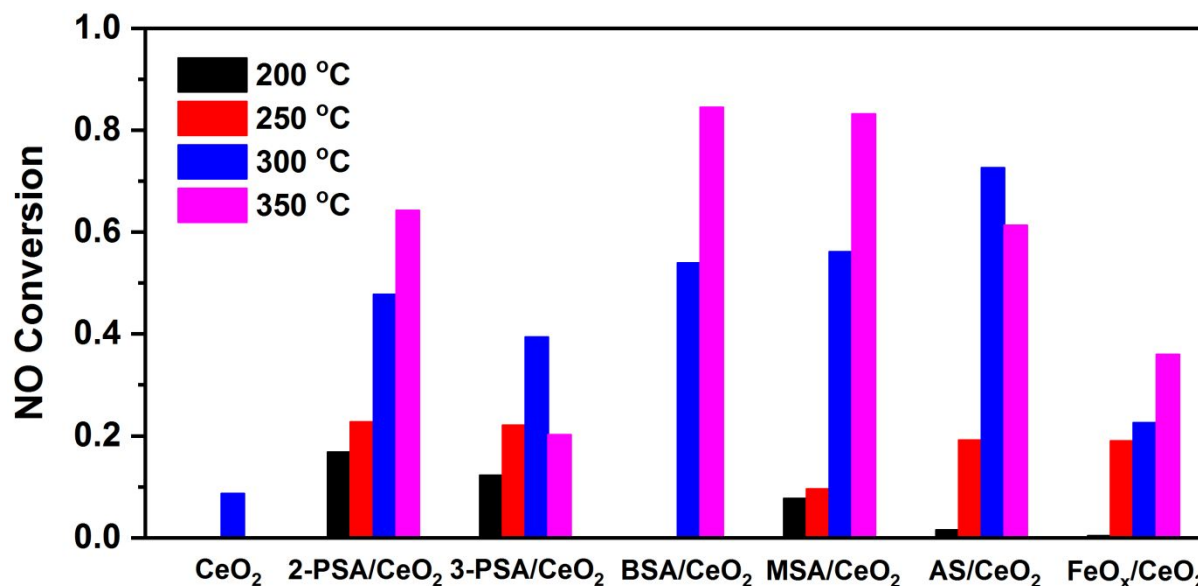
**Figure 3.** NH$_3$-SCR activities between 200 °C and 350 °C for bare CeO$_2$, sulfated CeO$_2$ synthesized using different S precursors, and FeO$_x$-promoted CeO$_2$. All sulfated CeO$_2$ catalysts exhibit higher activities than bare CeO$_2$ and FeO$_x$/CeO$_2$.

We also examined the activity of NH$_3$ oxidation, an important side reaction. Besides

consuming NH$_3$, it also generates NO gas, offsetting the NO conversion from NH$_3$-SCR. We

were not able to measure NH$_3$ conversion or N$_2$ production directly from the mass spectrometer

because of background interference, so here we only show NH$_3$-to-NO conversion calculated

from $m/z = 30$. No N$_2$O or NO$_2$ were detected, so the only other potential product besides NO

would be N$_2$. However, the NH$_3$-to-N$_2$ pathway is not likely to be important for NH$_3$ oxidation

because it is not active at this low surface coverage (see Discussion). This pathway is also not

significant for NH$_3$-SCR because, relative to the NH$_3$-to-NO pathway, it is less detrimental to the

SCR reaction (no NO generated). The results are exhibited as **Figure 4**, showing that bare CeO$_2$

is moderately active in this side reaction (18% conversion at 350 °C), and sulfates suppress its

activity (5% at 350 °C on 2-PSA/CeO$_2$). In contrast, FeO$_x$ significant enhances this side reaction,

with 18% conversion at only 250 °C, and 36% conversion at 350 °C. The high activity of

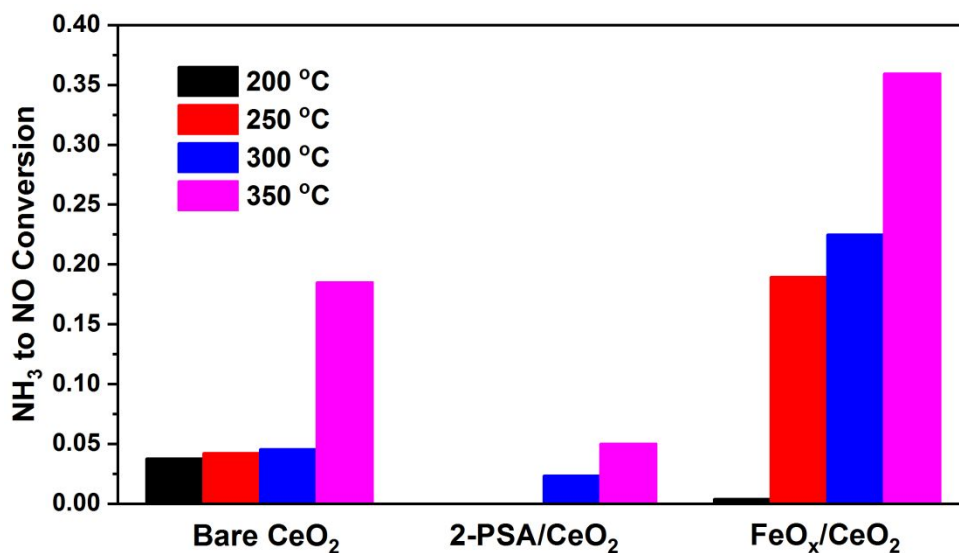FeO$_x$/CeO$_2$ on this side reaction partially explains its underwhelming high-temperature NH$_3$-SCR performance.



**Figure 4.** NH$_3$ oxidation activities of bare CeO$_2$, 2-PSA/CeO$_2$, and FeO$_x$/CeO$_2$ between 200 °C and 350 °C. The conversions presented in this figure only account for the NH$_3$-to-NO pathway.

## 3. Mechanistic investigation of the sulfate promotion effect by *in situ* DRIFTS

### 3.1. Adsorption of reactants on bare and promoted CeO$_2$

To understand the mechanism of the sulfate promotion effect, we performed a series of *in situ* DRIFTS experiments on bare CeO$_2$, 2-PSA/CeO$_2$, and 0.5% FeO$_x$/CeO$_2$. Other than the steady-state experiments, all *in situ* DRIFTS experiments were conducted at 250 °C, at which both 2-PSA (22% NO conversion) and FeO$_x$ (17% NO conversion) exhibit significant promotion effects.

The catalysts were first exposed to NH$_3$ gas at 250 °C in separate experiments, to investigate NH$_3$ adsorption on surfaces. Then each catalyst was purged with Ar, and DRIFT spectra were collected with Ar exposure time, to monitor adsorbates desorption. **Figure 5a** shows DRIFT

spectra after 30 min $NH_3$ exposure. The 1000-1800 $cm^{-1}$ region is shown here as it contains the most important features (see **Figure S5** for 2800-4000 $cm^{-1}$ region). No gas phase $NH_3$ vibrations can be observed due to low gas concentration (1000 ppm). On all catalysts, the main $NH_3$-derived adsorbate is $*NH_3$ on Lewis acid sites, represented by its symmetric bending peaks at 1168 and 1315 $cm^{-1}$, and a small asymmetric bending peak at 1602 $cm^{-1}$.[31, 49, 85-87] The split of the symmetric bending peak is common on oxide catalysts and likely from two types of Lewis acid sites.[31, 86, 87] N-H stretching peaks are also observed in the 3300 - 3600 $cm^{-1}$ region (**Figure S5**). The negative feature at 1355 $cm^{-1}$ is often observed and associated with $*NH_3$.[19, 88-90] No $*NH_4^+$ peak at around 1460 $cm^{-1}$ is found. $*NH_4^+$ is formed by $NH_3$ adsorption at Brønsted acid sites, and is a common $NH_3$-SCR intermediate on metal-exchanged zeolite catalysts.[24, 45, 47, 91] The absence of this peak indicates that on all catalysts, only Lewis acid sites are available for $NH_3$ adsorption, but not Brønsted acid sites, which disagrees with previous studies.[75] On 2-PSA/$CeO_2$, there is a small feature at 1550 $cm^{-1}$ assigned to $*NH_2$.[1, 7, 11, 92] It is generated by extracting one H atom from $*NH_3$ with surface O or other base sites. A negative feature is observed at ~1530 $cm^{-1}$ on $CeO_2$, which is repeatable and disappears when $NH_3$ desorbs, so it is likely associated with adsorbed $NH_3$ altering local bonding structure at oxygen vacancies.
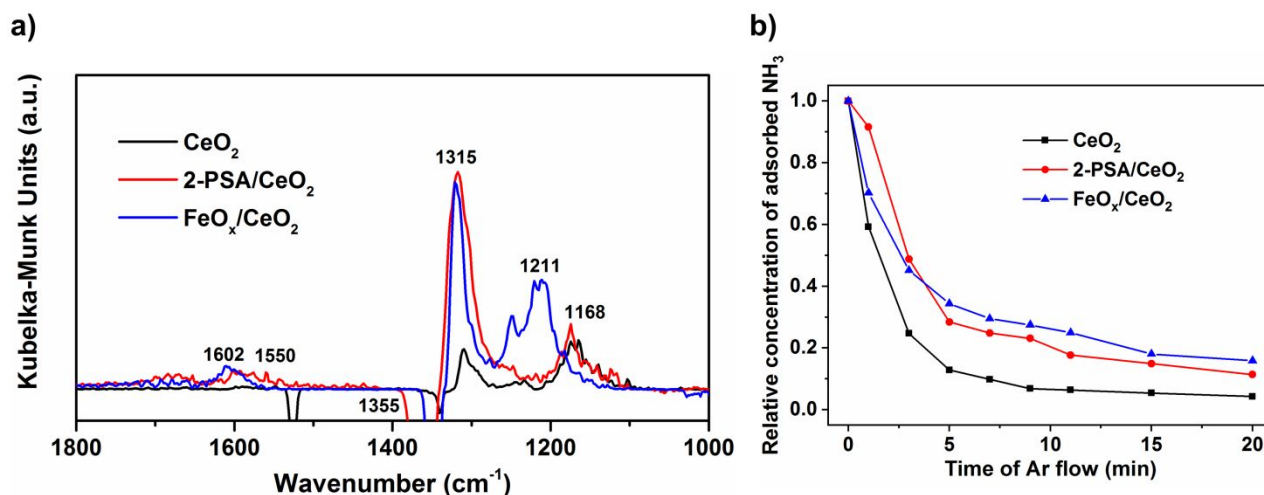
**Figure 5. (a)** DRIFT spectra for NH$_3$ adsorption on CeO$_2$, 2-PSA/CeO$_2$, and FeOx/CeO$_2$ after 30 min NH$_3$ exposure at 250 °C. **(b)** Surface concentration of *NH$_3$, relative to initial concentration, as a function of Ar purging time when purged with pure Ar, calculated from the integrated area between 1120-1340 cm$^{-1}$ for each spectrum (see **Figure S6**).

**Figure 5a** shows that all *NH$_3$ peaks are much stronger on 2-PSA/CeO$_2$ than bare CeO$_2$, suggesting more Lewis acid sites are created by surface sulfates for NH$_3$ adsorption, which is consistent with CO adsorption results (**Figure 2**). **Figure 5b** exhibits the relative concentration of *NH$_3$ remaining on surfaces under Ar purging, showing that *NH$_3$ desorbs more slowly from 2-PSA/CeO$_2$ than from bare CeO$_2$. Therefore, the overall strength of Lewis acid sites is increased by sulfates as well. Meanwhile, the presence of the small *NH$_2$ peak suggests H-extraction from *NH$_3$ is easier. **Figure 2** indicates surface O is deactivated by 2-PSA and another type of stronger base sites is likely created. Results on FeO$_x$/CeO$_2$ suggest FeO$_x$ has similar impacts on NH$_3$ adsorption with 2-PSA. Both the number of available Lewis acid sites and the binding strength are increased. A blue shift is observed for the 1168 cm$^{-1}$ symmetric bending peak. However, *NH$_2$ is not present on FeO$_x$/CeO$_2$.

We then investigated the adsorption of NO + $O_2$ on $CeO_2$, 2-PSA/$CeO_2$, and $FeO_x$/$CeO_2$ at 250 °C. **Figure 6a** shows DRIFT spectra after 30 min NO + $O_2$ exposure. Again, no NO (g) vibrations are observed due to low gas concentration (1000 ppm). No *NO (1800 ~ 2000 $cm^{-1}$) is observed as well.[93-95] The most abundant species on all three catalysts are nitrates (*$NO_3$) of different binding configurations. The $v_3$ vibration mode of *$NO_3$ is split into $v_3'$ mode (1500-1600 $cm^{-1}$) and $v_3''$ mode (1170-1300 $cm^{-1}$) when the symmetry is broken by binding with surface, and stronger binding leads to a larger split.[95, 96] Different components of the $v_3'$ peak clearly separate from each other, and we assign peaks at around 1596 $cm^{-1}$, 1562 $cm^{-1}$, and 1537 $cm^{-1}$ to bridging, bidentate, and monodentate *$NO_3$ respectively[1, 8, 35, 36, 95] (see **Table S2** for a summary of DRIFTS feature assignments). Two other small features at 1373 $cm^{-1}$ and 1010 $cm^{-1}$ are observed exclusively on bare $CeO_2$. They are likely from bidentate nitro (*O−N−O*) and nitrosyl (*$NO^-$) species, respectively.[45, 85, 95] These two species are not formed on $FeO_x$/$CeO_2$ or 2-PSA/$CeO_2$, potentially because structure around O vacancies is altered by $FeO_x$ and sulfates. A small shoulder assigned to molecularly adsorbed $NO_2$ (*$NO_2$, 1616 $cm^{-1}$) is also clearly observed on 2-PSA/$CeO_2$.[1, 32, 35, 58] Exposing catalysts to NO only without $O_2$ results in identical spectra, indicating active lattice oxygen of $CeO_2$ participates in NO binding.
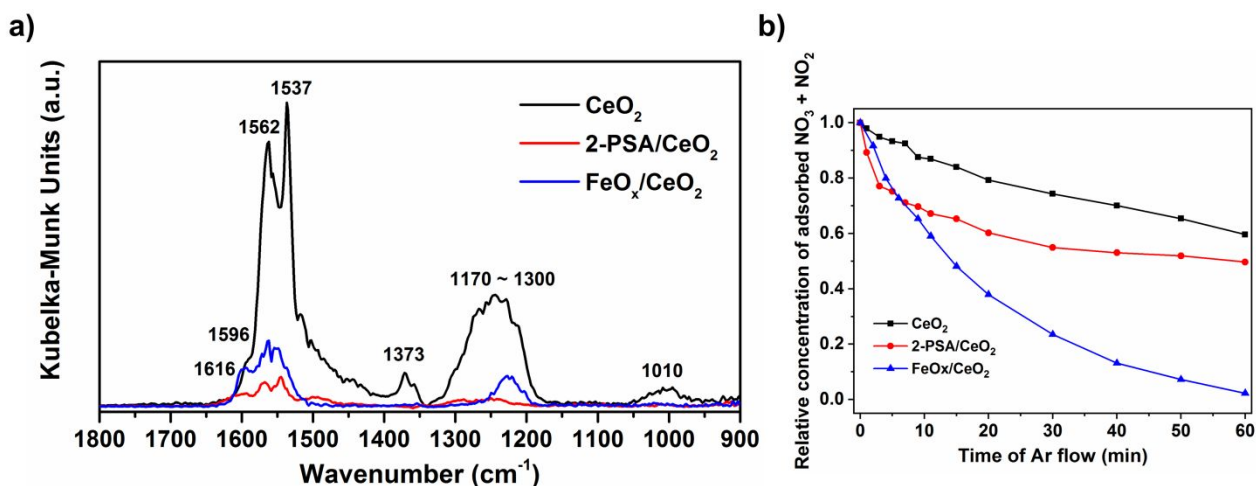
**Figure 6. (a)** DRIFT spectra of NO + $O_2$ adsorption on $CeO_2$, 2-PSA/$CeO_2$, and $FeO_x$/$CeO_2$ at 250 °C after 30 min NO + $O_2$ exposure. **(b)** Concentration (relative to initial concentration) of *$NO_3$ and *$NO_2$ remaining on each surface as a function of Ar purge time, calculated from the integrated area between 1400-1700 $cm^{-1}$ for each spectrum (see **Figure S7**).

Sulfate binding significantly reduces the number of NO binding sites on $CeO_2$ (by ~10 x, **Figure 6a**) and increases the fraction of *$NO_2$ and bridging *$NO_3$ among all adsorbates. As discussed below, *$NO_2$ is only a spectator during the reaction, but bridging *$NO_3$ is the most active species in the L-H mechanism. **Figure 6b** shows the relative concentration of *$NO_3$ (and *$NO_2$) remaining on surfaces during Ar purging calculated by integrating DRIFTS area between 1400 and 1700 $cm^{-1}$. It is also clear than surface sulfates weaken *$NO_3$ binding strength, as *$NO_3$ desorbs much faster from 2-PSA/$CeO_2$ than from bare $CeO_2$. The suppression and weakening of NO-$CeO_2$ binding are consistent with the deactivation of active surface O (**Figure 2**). It also makes adsorbates more mobile on the surface and easier to collide with other reactive species. $FeO_x$ affects NO adsorption in a similar way with sulfates, with a weaker impact in reducing the number of binding sites but a stronger impact in weakening the binding strength.

19

### 3.2.  Reactivity of *NO$_3$ with NH$_3$ (g)

To understand impacts of adsorbed sulfates on reactivity and reaction mechanism, transient experiments were performed at 250 °C. In separate experiments, bare CeO$_2$, 2-PSA/CeO$_2$, or FeO$_x$/CeO$_2$ was first exposed to NO + O$_2$ gas for 30 min to pre-adsorb *NO$_3$ and *NO$_2$ onto surfaces. Then, gas flow was switched to NH$_3$ (g) and DRIFT spectra were collected at different NH$_3$ exposure times to monitor evolution of surface species. We note that since *NO$_3$ and *NO$_2$ are pre-adsorbed onto catalyst surfaces, their reaction with NH$_3$ (g) in these experiments can only go through the L-H mechanism of the actual NH$_3$-SCR.

**Figure S8a** shows the NO-first transient DRIFT spectra on bare CeO$_2$. When flowing NH$_3$, *NO$_3$ gradually desorb from the surface as the intensities of their $v_3{'}$ and $v_3{''}$ peaks decrease slowly with time. No *NH$_3$ peaks appear, suggesting that NH$_3$ adsorption does not occur. **Figure S8b** compares the relative concentration of *NO$_3$ remaining on CeO$_2$ at different time when reacting with NH$_3$ (g) and when desorbing under Ar. *NO$_3$ disappears at similar rates under two situations, indicating they do not react with NH$_3$ (g). Also, no additional peaks from reaction intermediates or products are observed. Consequently, on bare CeO$_2$, pre-adsorbed *NO$_3$ does not react with NH$_3$ gas due to a lack of NH$_3$ adsorption sites, *i.e.*, the strong adsorption of *NO$_3$ poisons the surface by blocking NH$_3$ adsorption.

Results of the same experiments on 2-PSA/CeO$_2$ are presented in **Figure 7**. Different from bare CeO$_2$, *NH$_3$ peaks start to grow after 3 min NH$_3$ exposure and a new set of peaks that do not belong to *NH$_3$, *NO$_3$, or *NO$_2$ are observed at 1535 cm$^{-1}$, 1253 cm$^{-1}$, and 1120 cm$^{-1}$. Intensities of these peaks increase gradually with NH$_3$ exposure, indicating they are from reaction intermediates. According to literature, these peaks can be assigned to *NH$_2$NO$_2$. These peaks are still present even after 60 min, implying the decomposition of *NH$_2$NO$_2$ is very slow.

Meanwhile, both *NO$_2$ (1616 cm$^{-1}$) and bridging *NO$_3$ (1596 cm$^{-1}$) $v_3{'}$ peaks disappear quickly (within 5 min). Comparison between **Figure 7a** and **Figure S7b** reveals that the intensity of the *NO$_2$ peak drops at the same rate under NH$_3$ and Ar flow, so it simply desorbs without reacting with NH$_3$ (g). On the contrary, the bridging *NO$_3$ peak disappears much faster under NH$_3$ flow than Ar flow, indicating that it is highly reactive with NH$_3$ (g). Intensities of bidentate (1569 cm$^{-1}$) and monodentate *NO$_3$ (1544 cm$^{-1}$) $v_3{'}$ peaks also decrease, but not as fast as bridging *NO$_3$. **Figure 7b** shows the change in surface concentration of *NO$_3$/*NO$_2$ with time. Under NH$_3$ flow, the total amount of *NO$_3$/*NO$_2$ increases at the beginning due to the formation of *NH$_2$NO$_2$ 1535 cm$^{-1}$ peak (despite of *NO$_3$/*NO$_2$ desorption), and then decreases as *NO$_3$ desorption continues and *NH$_2$NO$_2$ potentially decomposes at a slow rate. The results presented above suggest that on sulfated CeO$_2$, NH$_3$ adsorption sites exist even if the surface is covered by pre-adsorbed *NO$_3$. The extra Lewis acid sites created by 2-PSA and weakened *NO$_3$ adsorption are crucial in this step. *NH$_3$ subsequently reacts with *NO$_3$ (bridging *NO$_3$ is most active), forming *NH$_2$NO$_2$ intermediate. However, the decomposition of *NH$_2$NO$_2$ is very slow at 250 °C, which accumulates on the surface and limits the reaction rate.
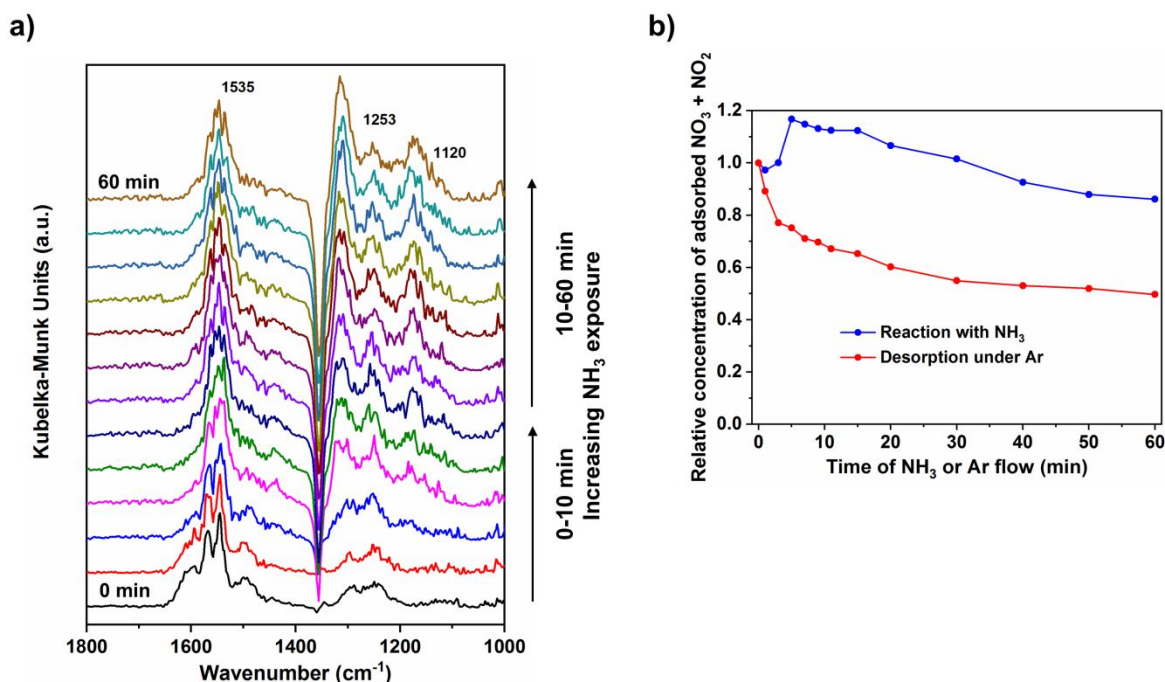
**Figure 7.** NO-first transient experiment on 2-PSA/CeO$_2$. **(a)** After NO + O$_2$ exposure for 30 min, DRIFT spectra were collected after various NH$_3$ exposure times From bottom to top, spectra were collected after 0, 1, 3, 5, 7, 9, 11, 15, 20, 30, 40, 50, and 60 min NH$_3$ exposure. **(b)** Concentration (relative to initial concentration) of *NO$_3$ and *NO$_2$ (integration of peak area 1400-1700 cm$^{-1}$) on the 2-PSA/CeO$_2$ surface when reacting with NH$_3$ (blue) compared to desorption under Ar (red).

**Figure 8** shows the results of the same experiment (NO flow first, then NH$_3$) as **Figure 7**, except for FeO$_x$/CeO$_2$ instead of 2-PSA/CeO$_2$. Again, *NH$_3$ peaks gradually appear after 3 min NH$_3$ exposure. The intensities of all *NO$_3$ peaks decrease much faster when reacting with NH$_3$ (g) (**Figure 8a**) than when desorbing under Ar (**Figure S7c**), suggesting *NO$_3$ are highly reactive towards NH$_3$ (g). The relative activities among the three nitrate configurations has the same trend, but with stronger differences, on FeO$_x$/CeO$_2$ as on 2-PSA/CeO$_2$: bridging *NO$_3$ (1591 cm$^{-1}$) > bidentate *NO$_3$ (1560 cm$^{-1}$) > monodentate *NO$_3$ (1548 cm$^{-1}$). The *NH$_2$NO$_2$ peaks (1531 cm$^{-1}$ and 1238 cm$^{-1}$, the ~1120 cm$^{-1}$ peak is too small) are also observed initially, but their intensities drop to 0 after 30 min of NH$_3$ exposure. This indicates that the reaction

between *NO$_3$ and *NH$_3$ on FeO$_x$/CeO$_2$ also yield *NH$_2$NO$_2$ intermediate, but unlike on 2-PSA/CeO$_2$, it goes through fast decomposition at 250 °C. The nitrate reaction under NH$_3$ flow and the *NH$_2$NO$_2$ decomposition contribute to the fast decrease in adsorbed nitrate, relative to the control experiment under Ar (**Figure 8b**). There is no initial increase as in **Figure 8b** because of a faster *NO$_3$ consumption rate and little accumulation of *NH$_2$NO$_2$ intermediate due to quick decomposition. Therefore, on FeO$_x$/CeO$_2$, the reaction between pre-adsorbed *NO$_3$ and NH$_3$ (g) follows a similar mechanism with sulfated CeO$_2$ but is much faster.
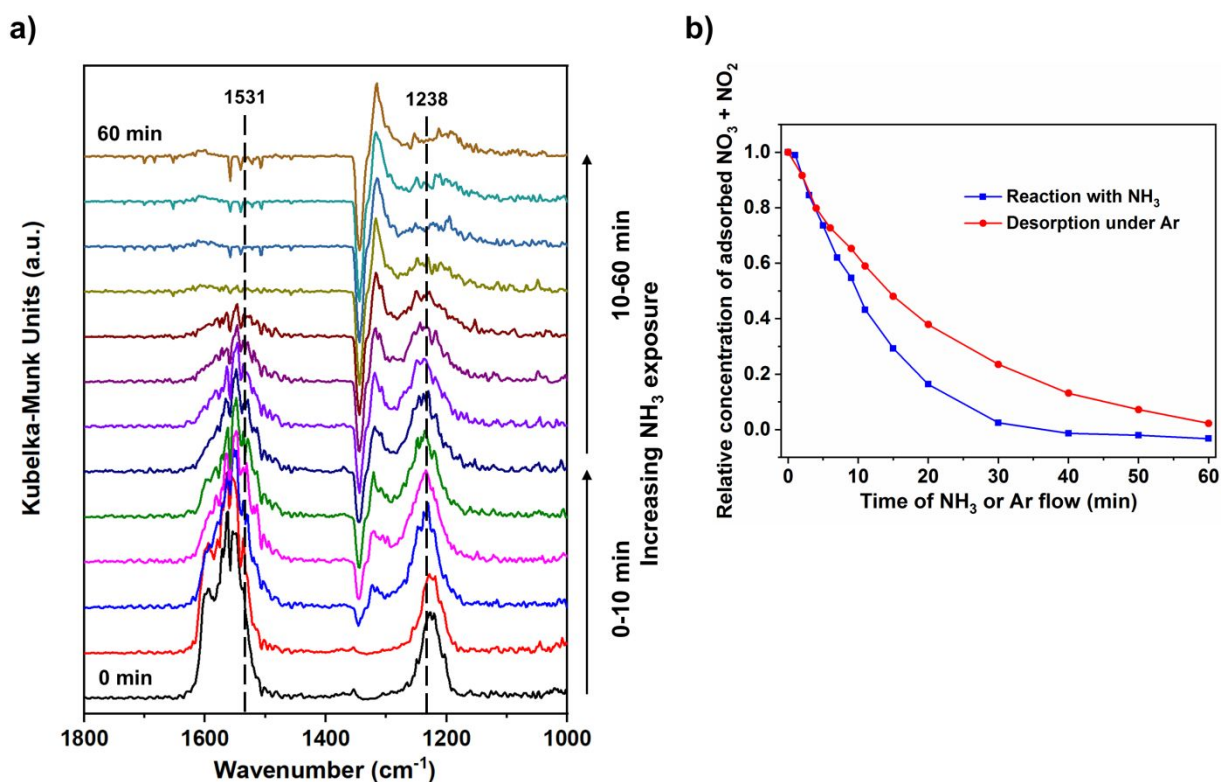


**Figure 8.** NO-first transient experiment on FeO$_x$/CeO$_2$. **(a)** After NO + O$_2$ exposure for 30 min, DRIFT spectra were collected at various NH$_3$ exposure times. From bottom to top, spectra were collected after 0, 1, 3, 5, 7, 9, 11, 15, 20, 30, 40, 50, and 60 min NH$_3$ exposure. **(b)** Concentration (relative to initial concentration) of *NO$_3$ and *NO$_2$ (integration of peak area 1400-1700 cm$^{-1}$) on the FeO$_x$/CeO$_2$ surface when reacting with NH$_3$ (blue) compared to desorption under Ar (red).

### 3.3. Reactivity of *NH₃ with NO + O₂

The NO-first transient experiments provide insight into how sulfates and $FeO_x$ promote the L-H mechanism of $NH_3$-SCR, but do not address the E-R mechanism since the NO is pre-adsorbed and cannot react in gas phase. Therefore, we also conducted $NH_3$-first transient experiments. Catalysts were exposed first to $NH_3$ (g) for 30 min, then to NO + $O_2$. DRIFT spectra were collected with NO + $O_2$ exposure time to probe the reactivity of *$NH_3$ with NO + $O_2$, which can occur through both L-H and E-R mechanisms. On 2-PSA/$CeO_2$, all *$NH_3$ and *$NH_2$ peaks disappear quickly (in 3 min), while *$NO_3$ and *$NO_2$ peaks grow gradually (over 30 min) (**Figure 9a**). *$NH_3$ peaks drop faster under NO + $O_2$ than under Ar (**Figure S9a**), indicating part of *$NH_3$ leaves the surface by reacting with NO (it is not likely that *$NH_3$ is consumed by reacting with $O_2$, as **Figure 4** shows 2-PSA/$CeO_2$ does not exhibit $NH_3$ oxidation activity at 250 °C). On *$NH_3$-covered 2-PSA/$CeO_2$, *$NO_3$ and *$NO_2$ form at a slower rate than on a clean one (without *$NH_3$) (**Figure S10a**), also suggesting in the first couple of minutes, NO is partially consumed by reacting with *$NH_3$. *$NH_3$ and intermediates may also block some NO adsorption sites, contributing to the slower adsorption rate. Despite evidence suggesting that *$NH_3$ is consumed by reacting with NO, no peaks for *$NH_2NO_2$, the slow-decomposing intermediate from the L-H mechanism, are identified in **Figure 9a**, suggesting the reaction is dominated by the E-R mechanism. *$NH_2$ is one important intermediate of this mechanism. No other intermediates are identified, probably because they quickly desorb or decompose with a short lifetime and surface coverage below detection limits (see Discussion).
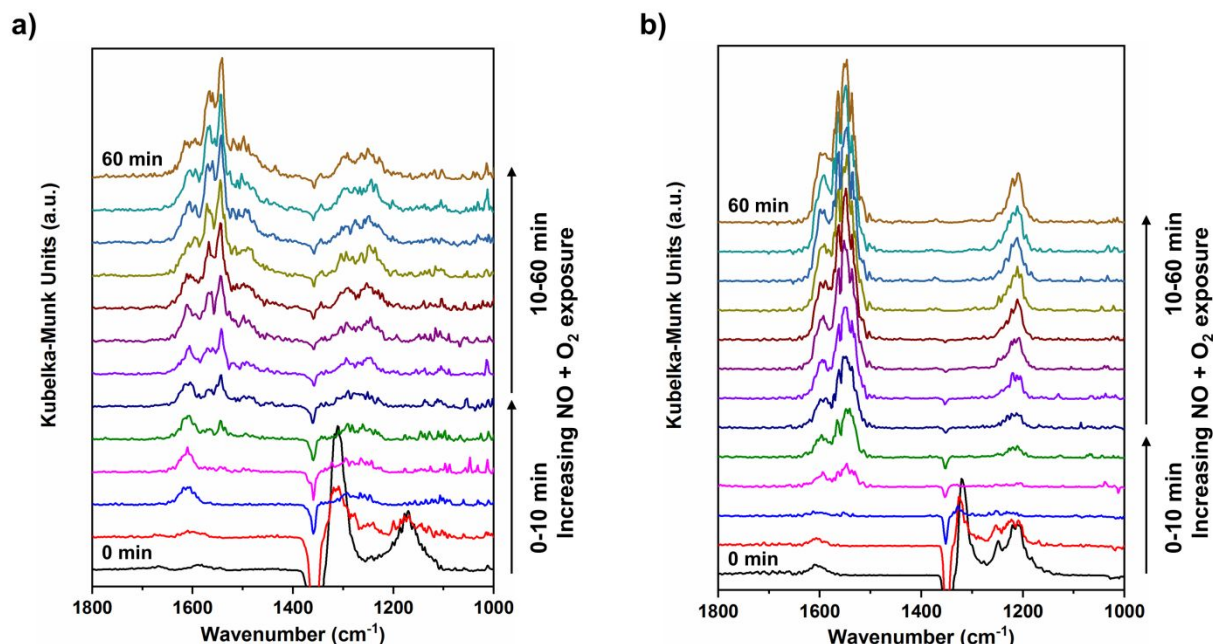
**Figure 9.** DRIFTS during NH$_3$-first transient experiments on **(a)** 2-PSA/CeO$_2$ and **(b)** FeO$_x$/CeO$_2$. Note the rapid decrease in *NH$_3$ (1168 and 1315 cm$^{-1}$) and *NH$_2$ (1550 cm$^{-1}$) and the rise in *NO$_3$ (1170-1300 and 1500-1600 cm$^{-1}$) and *NO$_2$ (1616 cm$^{-1}$). From bottom to top, spectra were collected after 0, 1, 3, 5, 7, 9, 11, 15, 20, 30, 40, 50, and 60 min NO + O$_2$ exposure.

**Figure 9b** shows results of the same experiments on FeO$_x$/CeO$_2$, which are similar with 2-PSA/CeO$_2$: *NH$_3$ peaks (no *NH$_2$ is observed on FeO$_x$/CeO$_2$) disappear faster than under Ar (**Figure S9b**), the formation of *NO$_3$ is slower than on a clean surface (**Figure S10b**), and no *NH$_2$NO$_2$ is observed. Therefore, on FeO$_x$/CeO$_2$, *NH$_3$ also reacts with NO + O$_2$, but not mainly through the L-H mechanism of NH$_3$-SCR. However, different from 2-PSA/CeO$_2$, FeO$_x$/CeO$_2$ has significant activity in NH$_3$ oxidation at 250 °C. Consequently, although **Figure 9a** and **9b** show that *NH$_3$ is consumed at a similar rate on 2-PSA/CeO$_2$ and FeO$_x$/CeO$_2$, 2-PSA/CeO$_2$ is more selective towards the E-R mechanism of NH$_3$-SCR, and more *NH$_3$ is oxidized on FeO$_x$/CeO$_2$.

*4.   Mechanistic discussions*

*4.1. Mechanistic insights into promotion effect of surface sulfate*

Based on results presented above, sulfated $CeO_2$ exhibits significantly higher $NH_3$-SCR activity than bare $CeO_2$. Mechanistic studies indicate that both L-H and E-R mechanisms exist simultaneously on sulfated $CeO_2$. The reaction network of relevant N-containing surface species is summarized as **Scheme 2**, and elementary steps for both mechanisms are shown as **Table 2**. Note that we never observed Brønsted acid sites participating in the reaction (no formation of $*NH_4^+$) on any of our catalysts, so both mechanisms here occur on Lewis acid sites through an $*NH_3$ intermediate. We are also confident that the fast-SCR through $*NO_2$ does not have significant contribution, and hence it is not included.
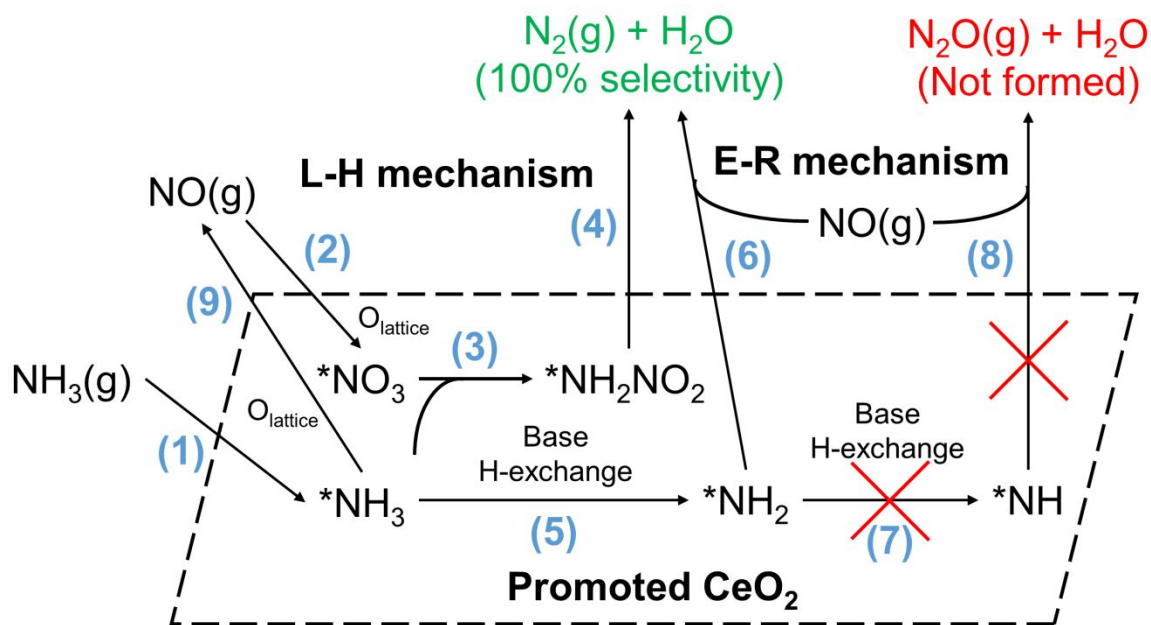


**Scheme 2.** A simplified $NH_3$-SCR reaction network on promoted $CeO_2$ including relevant N-containing species showing Langmuir-Hinshelwood and Eley-Rideal mechanisms. Although the formation of $N_2O$ was not observed on the catalysts reported in this work, we included steps leading to its formation on other SCR catalysts (Steps 7 and 8) to aid the discussion.

**Table 2.** Elementary steps in $NH_3$-SCR on promoted $CeO_2$.

| Langmuir-Hinshelwood Mechanism | | Eley-Rideal Mechanism | |
|---|---|---|---|
| $NH_3 (g) + * \rightarrow *NH_3$ | (1) | $NH_3 (g) + * \rightarrow *NH_3$ | (1) |
| $NO (g) + 2 O_{lattice} \rightarrow *NO_3$ | (2) | $*NH_3 + O_{lattice} \rightarrow *OH + *NH_2$ | (5) |
| $*NO_3 + *NH_3 \rightarrow *NO_2NH_2 + *OH$ | (3) | $*NH_2 + NO (g) \rightarrow N_2 (g) + H_2O$ | (6) |
| $*NO_2NH_2 \rightarrow N_2 (g) + *H_2O + O_{lattice}$ | (4) | $*NH_2 + O_{lattice} \rightarrow *NH + *OH$ | (7) |
| $2 *OH \rightarrow H_2O + O_{lattice}$ | | $*NH + NO (g) + O_{lattice} \rightarrow N_2O (g) + *OH$ | (8) |
| $O_2 (g) \rightarrow 2 O_{lattice}$ | | $2 *OH \rightarrow H_2O + O_{lattice}$ | |
| | | $O_2(g) \rightarrow 2 O_{lattice}$ | |

Numbers in brackets match numbers of corresponding steps in **Scheme 2**. $N_2O$ production resulting from Steps 7 and 8 was not observed for the catalysts reported in this work, but these steps are included here for comparison with other SCR catalysts.

The L-H mechanism on sulfated $CeO_2$ (2-PSA/$CeO_2$) is consistent with the current general view: N−N coupling occurs between $*NH_3$ and $*NO_3$ (step 3), and the intermediate $*NH_2NO_2$ further decomposes into $N_2$ and $H_2O$ (step 4). Some $*NO_2$ does form from NO (g) adsorption, but it does not react with $NH_3$ as it disappears at the same rate under $NH_3$ (**Figure 7a**) and Ar (**Figure S7b**). Consequently, it is a spectator, and fast-SCR is not important. The intensity of bridging $*NO_3$ peak drops significantly faster in **Figure 7a** than **Figure S7b**, proving it is the active species. Bidentate and monodentate $*NO_3$ are also active, though not as active as bridging ones. Active lattice oxygen from $CeO_2$ participates in the formation of $*NO_3$ and leave the surface later. The vacancy is filled by $O_2$ gas in a Mars-van-Krevelen manner. Therefore, the reducibility of oxide is desired for this mechanism.

The promotion of the L-H mechanism by surface sulfates mainly originates from more balanced and favored reactant adsorption. 2-PSA/CeO$_2$ has much more abundant Lewis acid sites to form *NH$_3$ (step 1) than bare CeO$_2$, and the adsorption is stronger (**Figure 5**). Meanwhile, surface sulfates decrease the number of *NO$_3$ binding sites (step 2), due to the deactivation of surface O (**Figure 6**), and the adsorption is weaker. On bare CeO$_2$, NO (g) adsorption is so dominating over NH$_3$ (g) that, under reaction conditions, the ratio between *NO$_3$ and *NH$_3$ deviates significantly from the stoichiometry of their reaction (1:1, step 3). Therefore, the L-H mechanism rate is slow. This is supported by **Figure S8a**, which reveals that at 250 °C, the adsorption of NH$_3$ (g) does not even occur on *NO$_3$-covered CeO$_2$. This problem is alleviated by the tuning of reactant adsorption by sulfates, as **Figure 7a** exhibits that on *NO$_3$-covered 2-PSA/CeO$_2$, NH$_3$ (g) could adsorb as *NH$_3$ (step 2), and further react with *NO$_3$ yielding *NH$_2$NO$_2$ (step 3). The steady-state ratio between *NH$_3$ and *NO$_3$ is closer to their reaction stoichiometry, which facilitates step 3. However, the overall L-H turnover rate on 2-PSA/CeO$_2$ is limited by the slow decomposition of *NH$_2$NO$_2$ (step 4, **Figure 7a**). **Figure S11** proves that step 4 is the rate-determining step at 250 °C, as *NH$_2$NO$_2$ accumulates under steady-state. It also shows that *NH$_3$ still exists even when *NO$_3$ is completely consumed, which supports that on sulfated CeO$_2$ surfaces, *NO$_3$ does not dominate over *NH$_3$ as it does on bare CeO$_2$.

The E-R mechanism generates N$_2$ and H$_2$O through the reaction between *NH$_2$ and NO (g) (step 6). We believe that the contribution of the E-R mechanism to NH$_3$-SCR activity is non-negligible for two reasons. First, the decomposition of *NH$_2$NO$_2$ (step 4) at 250 °C is extremely slow, so the L-H mechanism is unlikely to account for the 23% NO conversion at this temperature. Second, in the NH$_3$-first transient experiment (**Figure 9a**), *NH$_3$ is quickly consumed under NO + O$_2$ flow, though we do not observe the L-H intermediate *NH$_2$NO$_2$. The

N-coupling intermediates in this step are believed to decompose very quickly,[1, 28, 97, 98] and hence cannot be detected by DRIFTS (**Figure 9a**). Considering the low $NH_3$ oxidation activity of 2-PSA/CeO$_2$ at 250 °C (**Figure 4**), SCR through the E-R mechanism is likely to be responsible for most of the *$NH_3$ consumption. We note that it does not imply that the E-R mechanism is the dominating mechanism under steady-state, as in this experiment the surface was initially covered by *$NH_3$ and may not have many NO adsorption sites available, which is not the case under steady-state conditions.

Our results show that surface sulfates from 2-PSA also promote the E-R mechanism, by enhancing the formation of *$NH_3$ and *$NH_2$. As mentioned before, on bare CeO$_2$, step 1, the formation of *$NH_3$ from $NH_3$ (g), is very limited. This step is much more favored on 2-PSA/CeO$_2$ due to the presence of more, stronger Lewis acid sites, leading to higher *$NH_3$ coverage. Meanwhile, $NH_3$ (g) exposure does not generate any *$NH_2$ on bare CeO$_2$, but does on 2-PSA/CeO$_2$ (**Figure 5**). This suggests the thermodynamic equilibrium of step 5, the H-extraction from *$NH_3$, is shifted towards *$NH_2$ after 2-PSA deposition and activation, which is potentially done by modifying surface basicity. We think 2-PSA is likely to achieve this by creating a different type of basic sites from its fragments because **Figure 2** suggests that it actually deactivates basic surface O. Higher coverages of *$NH_3$ and *$NH_2$ on sulfated CeO$_2$ accelerate the E-R turnover rate. We recognize that even on 2-PSA/CeO$_2$, *$NH_2$ still has a low surface coverage at equilibrium compared with *$NH_3$ (**Figure 5**), which limits the E-R turnover rate. Under steady-states, this equilibrium can be constantly driven towards *$NH_2$ side by the quick reaction between *$NH_2$ and NO (g) (step 6). Nonetheless, this unfavored equilibrium is advantageous for selectivity, as no *NH, the further H-extraction product from *$NH_2$ (step 7), is

observed. Therefore, the reaction between *NH and NO (g) (step 8) generating by-product $N_2O$ does not occur, leading to 100% $N_2$ selectivity on all catalysts.

Besides promoting both mechanisms of $NH_3$-SCR, we also found out that surface sulfates suppress the activity of $NH_3$ oxidation (**Figure 4**). As previously mentioned, this side reaction has two-fold negative impacts: competing with $NH_3$-SCR for *$NH_3$, and offsetting NO conversion. Out of oxidation products $N_2$, $N_2O$, NO, and $NO_2$ that might be expected from this reaction,[50-52] $N_2O$ and $NO_2$ were not detected from our experiment. The detection of $N_2$ is difficult with our mass spectrometer due to high background levels, but the $NH_3$-to-$N_2$ pathway requires the coupling of *$NH_2$ or *NH species.[97, 99, 100] This step is difficult on our catalysts, as the coverage of *$NH_2$ is very low, and we did not observe any coupling intermediates from DRIFTS. Therefore, we believe that NO is the dominating oxidation product, and include $NH_3$-to-NO conversion as a single step 9, which is a simplified way to represent this side reaction. **Figure 4** suggests $NH_3$ oxidation becomes important at high temperature, and surface sulfates suppress its activity. Note that sulfates actually increase *$NH_3$ coverage. However, this effect is outweighed by the deactivation of active surface O, so overall this side reaction, step 9, is suppressed.

### 4.2. Comparison between surface sulfates and FeOx promoter

Small concentrations of transition metal oxide are known to promote $NH_3$-SCR activity of $CeO_2$,[29, 61, 63] but our results show that sulfate is a more effective promoter than $FeO_x$, especially at high temperature (**Figure 3**). Mechanistic investigations reveal that $FeO_x/CeO_2$ share similar reaction mechanisms with 2-PSA/$CeO_2$: both L-H and E-R mechanisms contribute to the

activity, no Brønsted acid participates in the reaction, and fast-SCR is not significant. Therefore, **Scheme 2** and **Table 2** can also be applied to $FeO_x/CeO_2$.

Our results show similarities between the function of $FeO_x$ and surface sulfates. They both modify surface acidity, enhancing $NH_3$ (g) adsorption to a similar extent (**Figure 5**) and reduce the number of adsorption sites and adsorption strength of $*NO_3$ (**Figure 6**). In the NO-first transient experiment, the formation of $*NH_3$ and then $*NH_2NO_2$ was observed as well (**Figure 8**). These results suggest that $FeO_x$ and sulfates promote the L-H mechanism in a similar manner: balancing the surface coverage of $*NH_3$ and $*NO_3$ by facilitating step 1 and suppressing step 2 (**Scheme 2**). A more favored step 1 also benefits the E-R mechanism, as discussed above in the 2-PSA/CeO$_2$ case.

$FeO_x/CeO_2$ seems to have a faster L-H turnover rate than 2-PSA/CeO$_2$ at 250 °C because of a much faster decomposition rate of $*NH_2NO_2$ (step 4, **Figure 8** compared with **Figure 7**). Steady-state DRIFTS at 250 °C shows no accumulation of $*NH_2NO_2$ on $FeO_x/CeO_2$, but strong features from $*NH_3$ and $*NO_3$ (**Figure S11**), suggesting step 3 is the rate-determining step on $FeO_x/CeO_2$ instead of step 4, as on 2-PSA/CeO$_2$. In spite of the faster rate for step 4, $FeO_x$ is a less effective promoter than sulfates for the following reasons. First, $FeO_x$ does not shift the equilibrium between $*NH_3$ and $*NH_2$ (step 5) as significantly as 2-PSA. This is supported by **Figure 5a**, showing that $NH_3$ (g) exposure does not generate DRIFTS-detectable amount of $*NH_2$ on $FeO_x/CeO_2$. The surface coverage of $*NH_2$ is lower on $FeO_x/CeO_2$ than 2-PSA/CeO$_2$, which limits the E-R turnover rate. Second, $FeO_x$ also increases $NH_3$ oxidation rate (**Figure 4**). At 350 °C, 36% of $NH_3$ is converted to NO on $FeO_x/CeO_2$ when there is no competition from $NH_3$-SCR, compared with 18% on bare CeO$_2$ and only 5% on 2-PSA/CeO$_2$. Both $FeO_x$ and sulfates enhance step 1 and increase the $*NH_3$ surface coverage, but $FeO_x$ does not deactivate surface O

as 2-PSA does. On the contrary, it likely introduces more active O at the $FeO_x/CeO_2$ interface,[101-103] increasing the rate of step 9. Third, at high temperature, the L-H turnover rate on $FeO_x/CeO_2$ might be lower than on 2-PSA/$CeO_2$, despite of faster *$NH_2NO_2$ decomposition. At 300 °C, *$NH_2NO_2$ does not accumulate on 2-PSA/$CeO_2$ under steady-state as it does at 250 °C (**Figure S11**). Therefore, the rate of step 4 is highly sensitive to temperature, and it does not limit the overall L-H turnover rate on 2-PSA/$CeO_2$ anymore at 300 °C. **Figure S11** also shows that on both $FeO_x/CeO_2$ and 2-PSA/$CeO_2$, *$NO_3$ is almost completely consumed, but residual *$NH_3$ features are stronger on $FeO_x/CeO_2$. This suggests that the *$NH_3$/*$NO_3$ coverage ratio under steady-state is likely more appropriate for step 3 on 2-PSA/$CeO_2$. Consequently, when step 4 becomes fast enough on both catalysts at high temperature, it is possible that 2-PSA/$CeO_2$ exhibits a higher L-H turnover rate.

**Conclusions**

The promotion effect of surface sulfates in $CeO_2$-catalyzed $NH_3$-SCR was investigated in detail. Sulfated $CeO_2$ synthesized using various S precursors all exhibit promoted $NH_3$-SCR activity between 200 °C and 350 °C, and outperform inorganic promoter $FeO_x$, especially above 300 °C. The promotion effect exists regardless of oxygen vacancy concentration on $CeO_2$ and is also valid on $Fe_2O_3$ surfaces. *In situ* DRIFTS studies revealed that on sulfated $CeO_2$, both Langmuir-Hinshelwood and Eley-Rideal mechanisms contribute to the activity. The reaction occurs exclusively on Lewis acid sites through an *$NH_3$ intermediate, and the fast-SCR pathway does not contribute. The roles of sulfates are to create new, stronger Lewis acid sites and to deactivate surface oxygen. $NH_3$-SCR is facilitated because (1) enhanced $NH_3$ adsorption and suppressed NO adsorption generate a more favored *$NH_3$/*$NO_3$ ratio for the L-H mechanism, (2)

tuning $NH_3$ adsorption and $*NH_3/*NH_2$ equilibrium increases active intermediate coverage in the E-R mechanism, and (3) the $NH_3$ oxidation side reaction is suppressed due to surface oxygen deactivation. In comparison, although the L-H intermediate $*NH_2NO_2$ decomposes faster on $FeO_x/CeO_2$ than on sulfated ones, $FeO_x/CeO_2$ shows high $NH_3$ oxidation activity and incapability to alter the $*NH_3/*NH_2$ equilibrium, and hence it is not a promoter as effective as sulfates.

## Conflicts of interest

There are no conflicts to declare.

## Acknowledgements

## References

1.　　　T. H. Vuong, J. r. Radnik, J. Rabeah, U. Bentrup, M. Schneider, H. Atia, U. Armbruster, W. Grünert and A. Brückner, *ACS Catal.*, 2017, **7**, 1693-1705.

2.      Y. Cheng, W. Song, J. Liu, H. Zheng, Z. Zhao, C. Xu, Y. Wei and E. J. Hensen, *ACS Catal.*, 2017, **7**, 3883.

3.      X. Gao, Y. Jiang, Y. Zhong, Z. Luo and K. Cen, *J. Hazard. Mater.*, 2010, **174**, 734-739.

4.      L. Li, L. Zhang, K. Ma, W. Zou, Y. Cao, Y. Xiong, C. Tang and L. Dong, *Appl. Catal., B*, 2017, **207**, 366-375.

5.      M. Machida, M. Uto, D. Kurogi and T. Kijima, *Chem. Mater.*, 2000, **12**, 3158-3164.

6.      K. B. Nam, D. W. Kwon and S. C. Hong, *Appl. Catal., A*, 2017, **542**, 55-62.

7.      G. Qi, R. T. Yang and R. Chang, *Appl. Catal., B*, 2004, **51**, 93-106.

8.      W. Shan, F. Liu, H. He, X. Shi and C. Zhang, *Appl. Catal., B*, 2012, **115**, 100-106.

9.      Y. Shu, H. Sun, X. Quan and S. Chen, *J. Phys. Chem. C*, 2012, **116**, 25319-25327.

10.     D. Wang, Y. Peng, S. C. Xiong, B. Li, L. N. Gan, C. M. Lu, J. J. Chen, Y. L. Ma and J. H. Li, *Appl. Catal., B*, 2018, **221**, 556-564.

11.     H. Zheng, W. Song, Y. Zhou, S. Ma, J. Deng, Y. Li, J. Liu and Z. Zhao, *J. Phys. Chem. C*, 2017, **121**, 19859-19871.

12.     T. Boningari, A. Somogyvari and P. G. Smirniotis, *Ind. Eng. Chem. Res.*, 2017, **56**, 5483-5494.

13.     D. K. Pappas, T. Boningari, P. Boolchand and P. G. Smirniotis, *J. Catal.*, 2016, **334**, 1-13.

14.     T. Boningari and P. G. Smirniotis, *Current Opinion in Chemical Engineering*, 2016, **13**, 133-141.

15.     T. Boningari, P. R. Ettireddy, A. Somogyvari, Y. Liu, A. Vorontsov, C. A. McDonald and P. G. Smirniotis, *J. Catal.*, 2015, **325**, 145-155.

16. F. Liu, H. He, Z. Lian, W. Shan, L. Xie, K. Asakura, W. Yang and H. Deng, *J. Catal.*, 2013, **307**, 340-351.

17. M. H. Kim and T. H. An, *Res. Chem. Intermed.*, 2011, **37**, 1333.

18. M. D. Amiridis, R. V. Duevel and I. E. Wachs, *Appl. Catal., B*, 1999, **20**, 111-122.

19. A. Shi, X. Wang, T. Yu and M. Shen, *Appl. Catal., B*, 2011, **106**, 359-369.

20. N. H. Ahn, T. Ryu, Y. Kang, H. Kim, J. Shin, I. S. Nam and S. B. Hong, *ACS Catal.*, 2017, **7**, 6781-6785.

21. D. Zhang and R. T. Yang, *Appl. Catal., A*, 2017, **543**, 247-256.

22. S. H. Begum, C.-T. Hung, Y.-T. Chen, S.-J. Huang, P.-H. Wu, X. Han and S.-B. Liu, *J. Mol. Catal. A: Chem.*, 2016, **423**, 423-432.

23. L. Kovarik, N. M. Washton, R. Kukkadapu, A. Devaraj, A. Wang, Y. Wang, J. Szanyi, C. H. Peden and F. Gao, *ACS Catal.*, 2017, **7**, 2458-2470.

24. B. Li, Z. Huang, X. Huang, S. Kou, F. Liu, X. Zhang and H. Yang, *RSC Adv.*, 2016, **6**, 6300-6307.

25. H. Liu, J. Wang, T. Yu, S. Fan and M. Shen, *Catal. Sci. Technol.*, 2014, **4**, 1350-1356.

26. M. Schwidder, M. S. Kumar, U. Bentrup, J. Pérez-Ramírez, A. Brückner and W. Grünert, *Microporous Mesoporous Mater.*, 2008, **111**, 124-133.

27. P. S. Metkar, N. Salazar, R. Muncrief, V. Balakotaiah and M. P. Harold, *Appl. Catal., B*, 2011, **104**, 110-126.

28. G. Qi and R. T. Yang, *J. Phys. Chem. B*, 2004, **108**, 15738-15747.

29. P. A. Kumar, Y. E. Jeong and H. P. Ha, *Catal. Today*, 2017, **293**, 61-72.

30. D. W. Kwon, K. H. Park and S. C. Hong, *Chem. Eng. J.*, 2016, **284**, 315-324.
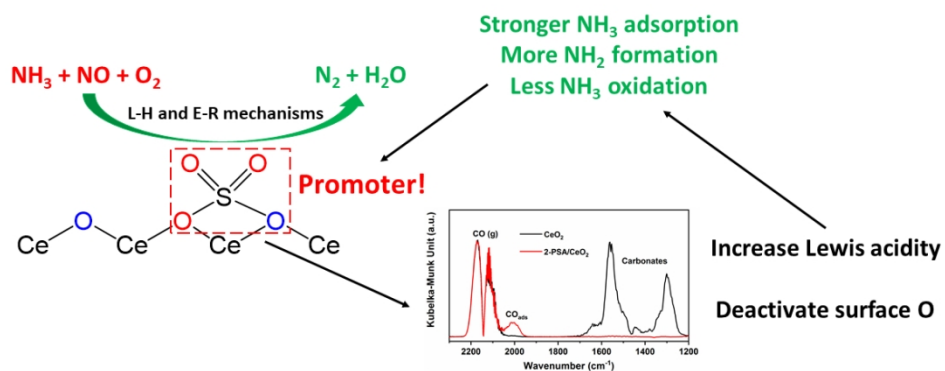
31.     L. Zhang, D. Wang, Y. Liu, K. Kamasamudram, J. Li and W. Epling, *Appl. Catal., B*, 2014, **156**, 371-377.

32.     V. Sanchez-Escribano, T. Montanari and G. Busca, *Appl. Catal., B*, 2005, **58**, 19-23.

33.     H. Huang, R. Long and R. Yang, *Appl. Catal., A*, 2002, **235**, 241-251.

34.     S. Yang, Y. Liao, S. Xiong, F. Qi, H. Dang, X. Xiao and J. Li, *J. Phys. Chem. C*, 2014, **118**, 21500-21508.

35.     C. Gao, J.-W. Shi, Z. Fan, Y. Yu, J. Chen, Z. Li and C. Niu, *Fuel Process. Technol.*, 2017, **167**, 322-333.

36.     D. Meng, W. Zhan, Y. Guo, Y. Guo, L. Wang and G. Lu, *ACS Catal.*, 2015, **5**, 5973-5983.

37.     S. Yang, Y. Guo, H. Chang, L. Ma, Y. Peng, Z. Qu, N. Yan, C. Wang and J. Li, *Appl. Catal., B*, 2013, **136**, 19-28.

38.     T. Boningari, D. K. Pappas and P. G. Smirniotis, *J. Catal.*, 2018, **365**, 320-333.

39.     D. Damma, T. Boningari, P. R. Ettireddy, B. M. Reddy and P. G. Smirniotis, *Ind. Eng. Chem. Res.*, 2018, **57**, 16615-16621.

40.     B. Thirupathi and P. G. Smirniotis, *J. Catal.*, 2012, **288**, 74-83.

41.     B. Thirupathi and P. G. Smirniotis, *Catal. Lett.*, 2011, **141**, 1399.

42.     P. M. Sreekanth, D. A. Peña and P. G. Smirniotis, *Ind. Eng. Chem. Res.*, 2006, **45**, 6444-6449.

43.     A. Liu, L. Yang, C.-H. Traulsen and J. Cornelissen, *Chem. Comm.*, 2017, **53**, 7632-7634.

44.     X. Yao, Z. Wang, S. Yu, F. Yang and L. Dong, *Appl. Catal., A*, 2017, **542**, 282-288.

45.     G. Zhou, B. Zhong, W. Wang, X. Guan, B. Huang, D. Ye and H. Wu, *Catal. Today*, 2011, **175**, 157-163.

46.     P. Chen, M. Jabłońska, P. Weide, T. Caumanns, T. Weirich, M. Muhler, R. Moos, R. Palkovits and U. Simon, *ACS Catal.*, 2016, **6**, 7696-7700.

47.     M. P. Ruggeri, A. Grossale, I. Nova, E. Tronconi, H. Jirglova and Z. Sobalik, *Catal. Today*, 2012, **184**, 107-114.

48.     L. Zhang, T. Du, H. Qu, B. Chi and Q. Zhong, *Chem. Eng. J.*, 2017, **313**, 702-710.

49.     D. Sun, Q. Liu, Z. Liu, G. Gui and Z. Huang, *Appl. Catal., B*, 2009, **92**, 462-467.

50.     R. Long and R. Yang, *J. Catal.*, 2001, **201**, 145-152.

51.     R. Q. Long and R. T. Yang, *Chem. Comm.*, 2000, 1651-1652.

52.     S. Imamura, A. Doi and S. Ishida, *Ind. Eng. Chem. Prod. Rd.*, 1985, **24**, 75-80.

53.     W. Shan, F. Liu, Y. Yu and H. He, *Chin. J. Catal.*, 2014, **35**, 1251-1259.

54.     S. Gillot, G. Tricot, H. Vezin, J.-P. Dacquin, C. Dujardin and P. Granger, *Appl. Catal., B*, 2017, **218**, 338-348.

55.     J. Han, J. Meeprasert, P. Maitarad, S. Nammuangruk, L. Shi and D. Zhang, *J. Phys. Chem. C*, 2016, **120**, 1523-1533.

56.     G. Carja, G. Delahay, C. Signorile and B. Coq, *Chem. Comm.*, 2004, 1404-1405.

57.     B. Shen, Y. Wang, F. Wang and T. Liu, *Chem. Eng. J.*, 2014, **236**, 171-180.

58.     R. Q. Long and R. T. Yang, *J. Am. Chem. Soc.*, 1999, **121**.

59.     K. B. Nam, D. W. Kwon and S. C. Hong, *Appl. Catal., A*, 2017.

60.     R. Ke, J. Li, X. Liang and J. Hao, *Catal. Comm.*, 2007, **8**, 2096-2099.

61.     J. W. Choung, I.-S. Nam and S.-W. Ham, *Catal. Today*, 2006, **111**, 242-247.

62.     D. Zhou, Z. Ren, B. Li, Z. Ma, X. Zhang and H. Yang, *RSC Adv.*, 2015, **5**, 31708-31715.

63.     S. T. Choo, S. D. Yim, I.-S. Nam, S.-W. Ham and J.-B. Lee, *Appl. Catal., B*, 2003, **44**, 237-252.

64.     L. Lietti, I. Nova and P. Forzatti, *Top. Catal.*, 2000, **11**, 111-122.

65.     L. Lietti, I. Nova, G. Ramis, L. Dall'Acqua, G. Busca, E. Giamello, P. Forzatti and F. Bregani, *J. Catal.*, 1999, **187**, 419-435.

66.     Z. Liu, H. Su, B. Chen, J. Li and S. I. Woo, *Chem. Eng. J.*, 2016, **299**, 255-262.

67.     L. Casagrande, L. Lietti, I. Nova, P. Forzatti and A. Baiker, *Appl. Catal., B*, 1999, **22**, 63-77.

68.     X. Du, X. Gao, W. Hu, J. Yu, Z. Luo and K. Cen, *J. Phys. Chem. C*, 2014, **118**, 13617-13622.

69.     D. Prieto-Centurion, T. R. Eaton, C. A. Roberts, P. T. Fanson and J. M. Notestein, *Appl. Catal., B*, 2015, **168**, 68-76.

70.     C. A. Roberts, D. Prieto-Centurion, Y. Nagai, Y. F. Nishimura, R. D. Desautels, J. Van Lierop, P. T. Fanson and J. M. Notestein, *J. Phys. Chem. C*, 2015, **119**, 4224-4234.

71.     C. A. Roberts, L. Savereide, D. J. Childers, T. C. Peck and J. M. Notestein, *Catal. Today*, 2016, **267**, 56-64.

72.     Z. Zhu, Z. Liu, H. Niu and S. Liu, *J. Catal.*, 1999, **187**, 245-248.

73.     P. Li, Z. Liu, Q. Li, W. Wu and Q. Liu, *Ind. Eng. Chem. Res.*, 2014, **53**, 7910-7916.

74.     G. Xie, Z. Liu, Z. Zhu, Q. Liu, J. Ge and Z. Huang, *J. Catal.*, 2004, **224**, 42-49.

75.     L. Ma, C. Y. Seo, M. Nahata, X. Chen, J. Li and J. W. Schwank, *Appl. Catal., B*, 2018, **232**, 246-259.

76.     D. L. Mowery, M. S. Graboski, T. R. Ohno and R. L. McCormick, *Appl. Catal., B*, 1999, **21**, 157-169.

77.     L. Chen, J. P. McCann and S. L. Tait, *Appl. Catal., A*, 2018, **549**, 19-30.

78.     D. Littlejohn and S.-G. Chang, *J. Electron. Spectrosc. Relat. Phenom.*, 1995, **71**, 47-50.

79.     D. L. Mowery and R. L. McCormick, *Appl. Catal., B*, 2001, **34**, 287-297.

80.     H. H. Kung, *Catal. Today*, 1992, **11**, 443-453.

81.     G. Busca, H. Saussey, O. Saur, J. C. Lavalley and V. Lorenzelli, *Appl. Catal.*, 1985, **14**, 245-260.

82.     Z. Si, D. Weng, X. Wu, J. Yang and B. Wang, *Catal. Comm.*, 2010, **11**, 1045-1048.

83.     C. Morterra, G. Cerrato and V. Bolis, *Catal. Today*, 1993, **17**, 505-515.

84.     C. Morterra, G. Cerrato, C. Emanuel and V. Bolis, *J. Catal.*, 1993, **142**, 349-367.

85.     H. Hu, K. Zha, H. Li, L. Shi and D. Zhang, *Appl. Surf. Sci.*, 2016, **387**, 921-928.

86.     I. Jimenez, M. Centeno, R. Scotti, F. Morazzoni, J. Arbiol, A. Cornet and J. Morante, *J. Mater. Chem.*, 2004, **14**, 2412-2420.

87.     R. Long and R. Yang, *J. Catal.*, 2000, **190**, 22-31.

88.     H. Zhu, J. H. Kwak, C. H. Peden and J. Szanyi, *Catal. Today*, 2013, **205**, 16-23.

89.     L. Ma, Y. Cheng, G. Cavataio, R. W. McCabe, L. Fu and J. Li, *Appl. Catal., B*, 2014, **156**, 428-437.

90.     H. Sjövall, E. Fridell, R. J. Blint and L. Olsson, *Top. Catal.*, 2007, **42**, 113-117.

91.     D. Klukowski, P. Balle, B. Geiger, S. Wagloehner, S. Kureti, B. Kimmerle, A. Baiker and J.-D. Grunwaldt, *Appl. Catal., B*, 2009, **93**, 185-193.

92.     M. Wallin, H. Grönbeck, A. L. Spetz and M. Skoglundh, *Appl. Surf. Sci.*, 2004, **235**, 487-500.

93.     G. Ramis, G. Busca, F. Bregani and P. Forzatti, *Appl. Catal.*, 1990, **64**, 259-278.

94.     M. Mihaylov, K. Chakarova and K. Hadjiivanov, *J. Catal.*, 2004, **228**, 273-281.

95.     G. Underwood, T. Miller and V. Grassian, *J. Phys. Chem. A*, 1999, **103**, 6184-6190.

96.     G. Busca and V. Lorenzelli, *J. Catal.*, 1981, **72**, 303-313.

97.    G. Ramis, L. Yi, G. Busca, M. Turco, E. Kotur and R. J. Willey, *J. Catal.*, 1995, **157**, 523-535.

98.    C. Paolucci, A. A. Verma, S. A. Bates, V. F. Kispersky, J. T. Miller, R. Gounder, W. N. Delgass, F. H. Ribeiro and W. F. Schneider, *Angew. Chem. Int. Ed.*, 2014, **53**, 11828-11833.

99.    L. Zhang and H. He, *J. Catal.*, 2009, **268**, 18-25.

100.   G. Ramis, L. Yi and G. Busca, *Catal. Today*, 1996, **28**, 373-380.

101.   D. Widmann and R. J. Behm, *Angew. Chem. Int. Ed.*, 2011, **50**, 10241-10245.

102.   A. Bueno-López, K. Krishna, M. Makkee and J. Moulijn, *J. Catal.*, 2005, **230**, 237-248.

103.   X. Zhu, K. Li, Y. Wei, H. Wang and L. Sun, *Energy Fuels*, 2014, **28**, 754-760.

330x127mm (96 x 96 DPI)